This is the pre-peer reviewed version of the following article:

Garcia-Cortadella R., Masvidal-Codina E., De la Cruz J.M., Schäfer N., Schwesig G., Jeschke C., Martinez-Aguilar J., Sanchez-Vives M.V., Villa R., Illa X., Sirota A., Guimerà A., Garrido J.A.. Distortion-Free Sensing of Neural Activity Using Graphene Transistors. Small, (2020). 16. 1906640: - . 10.1002/smll.201906640,

which has been published in final form at https://dx.doi.org/10.1002/smll.201906640. This article may be used for non-commercial purposes in accordance with Wiley Terms and Conditions for Use of Self-Archived Versions.

Article type: Full paper

Distortion-Free Sensing of Neural Activity Using Graphene Transistors

*Ramon Garcia-Cortadella, Eduard Masvidal-Codina, Jose de la Cruz, Nathan Schäfer, Gerrit Schwesig, Christoph Jeschke, Javier Martinez-Aguilar, Maria V. Sanchez-Vives, Rosa Villa, Xavi Illa, Anton Sirota, Anton Guimerà and Jose A. Garrido**

R. Garcia-Cortadella, J. de la Cruz, N. Schäfer, Prof. J. A. Garrido
Catalan Institute of Nanoscience and Nanotechnology (ICN2), CSIC and BIST, Campus UAB, Bellaterra, 08193 Barcelona, Spain
Email: joseantonio.garrido@icn2.cat
E. Masvidal-Codina, J. Martinez-Aguilar, Dr. R. Villa, Dr. X. Illa, Dr. A. Guimerà
Instituto de Microelectrónica de Barcelona, IMB-CNM (CSIC), Esfera UAB, Bellaterra, Spain
J. Martinez-Aguilar, Dr. R. Villa, Dr. X. Illa, Dr. A. Guimerà
Centro de Investigación Biomédica en Red en Bioingeniería, Biomateriales y Nanomedicina (CIBER-BBN), Madrid, Spain
C. Jeschke
Multi Channel Systems (MCS) GmbH, Reutlingen, Germany
M. Sanchez-Vives
Institut d'Investigacions Biomèdiques August Pi i Sunyer (IDIBAPS), Barcelona, Spain
G. Schwesig, Prof. A. Sirota
Bernstein Center for Computational Neuroscience Munich, Munich Cluster of Systems Neurology (SyNergy), Faculty of Medicine, Ludwig-Maximilians Universität München, Planegg-Martinsried, Germany
Prof. M. V. Sanchez-Vives, Prof. J. A. Garrido
ICREA, Pg. Lluís Companys 23, 08010 Barcelona, Spain

Keyword: harmonic distortion, frequency response, graphene, solution-gated, neural sensing

Graphene solution-gated field-effect transistors (g-SGFETs) are promising sensing devices to record *in-vivo* neural activity offering some advantages with respect to conventional micro-electrodes, including an increased sensitivity in the low frequency regime. However, distortion mechanisms in g-SGFET, which can affect signals of large amplitude or high frequency, have not been evaluated. Here, a detailed characterization and modelling of the harmonic distortion and non-ideal frequency response in g-SGFETs is presented. This accurate description of the input-output relation of the g-SGFETs allows to define the voltage and frequency dependent transfer functions, which can be used to correct distortions in the transduced signals. The effect of signal distortion and its subsequent calibration are shown for different types of electrophysiological signals; spanning from large amplitude and low frequency cortical spreading depression events to low amplitude and high frequency action potentials. The thorough description of the distortion mechanisms presented in this article demonstrates that g-SGFETs can be used as distortion-free signal transducers not only for neural sensing, but also for a broader range of applications in which g-SGFET sensors are used.

1. Introduction

Graphene has attracted much attention for its use in active sensors due to its high carrier mobility[1] and chemical stability.[2] Many applications have been explored, and more are under study, in which graphene is used to transduce the physical property of interest into an electrical signal. Prominent examples include biochemical sensors,[3–5] gas sensors,[6,7] pH sensors,[8,9] ion sensors[10] or transducers of electrical potential for neural interfaces.[11–13] The latter, has recently attracted increasing attention due to the potential of graphene solution-gated field-effect transistors to record infra-slow[14] brain activity with a high spatial resolution.[15] This capability opens the door to full-band neural activity sensing; from large amplitude infra-slow oscillations to small amplitude but faster signals such as local field potentials or action potentials.

In g-SGFETs, the graphene channel is in contact with an electrolyte, which comprises the gate of the g-SGFET (see **Figure 1**a). The electrochemical potential in the electrolyte can therefore be regarded as the gate-to-source voltage (V_{gs}), which couples with the channel through the graphene-electrolyte interface capacitance (C_{int}).[16,17] The electric field at the interface produces a change in the number of charge carriers in the graphene channel and therefore a variation in the drain-to-source current (I_{ds-sig}) for a constant drain-to-source bias (V_{ds}). These current changes are proportional to the signal at the gate (V_{gs-sig}) and to the transconductance (G_m) (see Figure 1b), which represents the input-output relation of the g-SGFET, also referred to as its transfer function. The G_m in g-SGFETs is, in a first approximation, proportional to the electrical mobility of graphene and C_{int} per unit area;[18] therefore presenting no dependence on the area of the active channel. This is the main cause for the improved sensitivity of g-SGFETs in the infra-slow frequency band in comparison with conventional micro-electrodes.[19]

Despite the great potential of g-SGFETs for full-band neural activity monitoring and other applications in sensing, the signal distortion introduced by these transducers remains a key aspect, which has been so far largely underestimated. Signal distortion can appear in any amplifying system due several reasons; including voltage dependent gain, which leads to harmonic distortion, frequency dependent gain that leads to different amplification of various frequency components and phase distortion due to a non-null imaginary part of the gain. In the specific case of the g-SGFET, a voltage or frequency dependence of G_m will lead to signal distortion. In the first place, non-linearities in the $I_{ds} - V_{gs}$ curves, lead to a dependence with

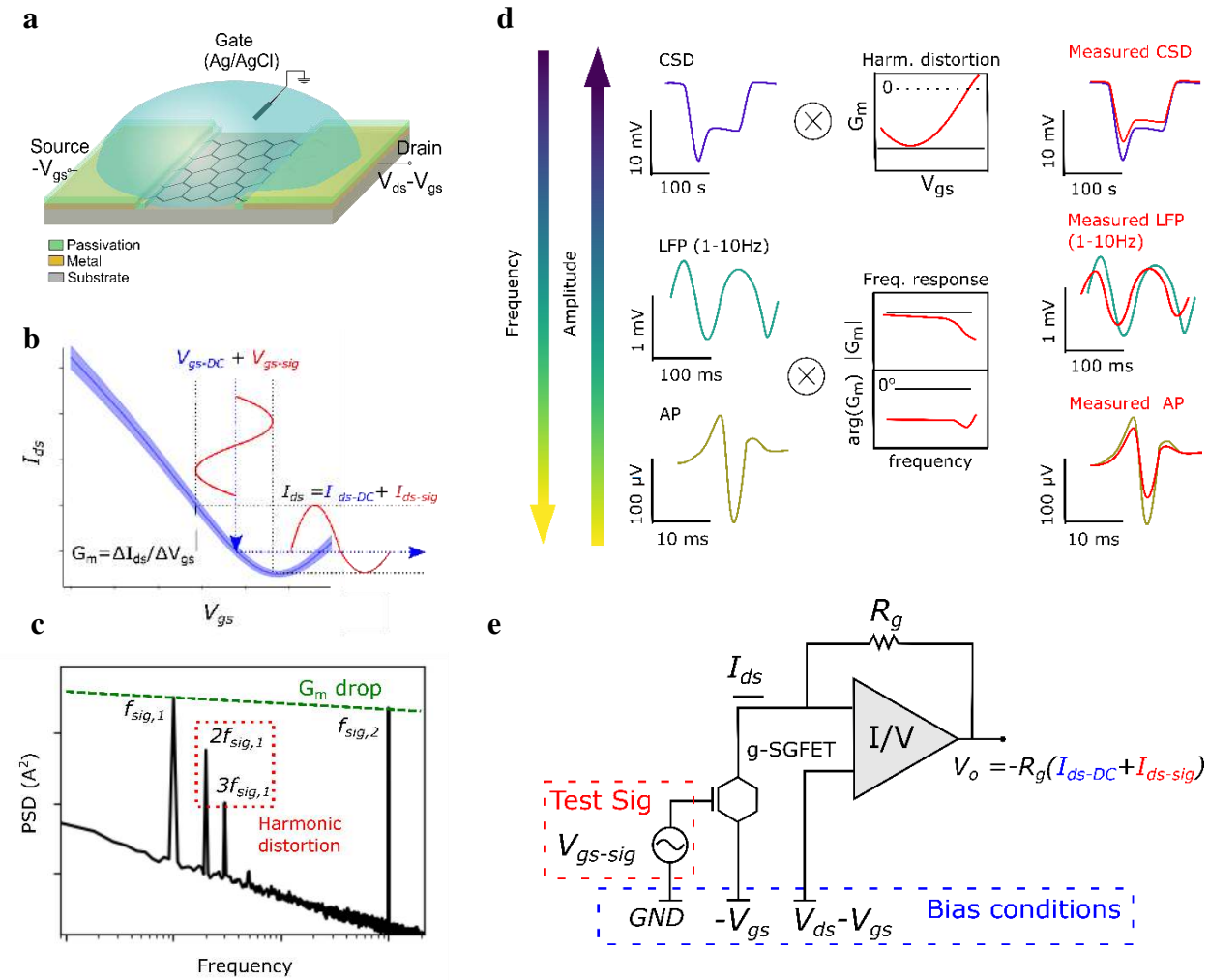

Figure 1: a) Drawing of a g-SGFET showing the graphene channel, metal contacts, SU8 passivation, electrolyte gate and reference electrode together with the applied bias. b) Typical transfer characteristics of a g-SGFET. G_m is indicated as $\Delta I_{ds}/\Delta V_{gs}$. c) Typical PSD of the distorted output signal of a g-SGFET. The two tones $f_{sig,1} =$ 10Hz and $f_{sig,2} =$ 1kHz illustrate the effect of transconductance attenuation at higher frequencies. The effect of harmonic distortion on the 10Hz signal results in the appearance of the harmonic components at $f = 2f_{sig}$ and $3f_{sig}$. d) Representation of a typical cortical spreading depression (CSD) event, local-field potential in the 1-10Hz band and an action potential. The original electrophysiological signal is multiplied by the G_m of the device which might present a V_{gs} dependence (centre-top), producing harmonic distortion shown in red (top-right), or a non-ideal frequency response (centre-bottom), producing frequency response distortion of the detected signals. e) Circuit diagram of the custom build electronic setup used for the characterization of g-SGFETs and recording of electrophysiological activity. The reference electrode is set at ground (GND), $-V_{gs}$ is applied between gate and source and $V_{ds} - V_{gs}$ between gate and drain. The current I_{ds} is preamplified by the current-to-voltage converter (I/V).

V_{gs} and therefore to harmonic distortion of the signal (see Figure 1b and 1c). The amplitude of the harmonics introduced can ideally be derived from the Taylor expansion of the I_{ds}-V_{gs} curves.

This description has been previously presented and evaluated for a GFET analytical model.[20] However, theoretically predicted parameters have never been compared to experimentally measured distortion levels in GFETs. Validating the relation between non-linearities in the I_{ds}-V_{gs} curves and harmonic distortion is critical to understand and mitigate its effect on the sensing capabilities of g-SGFETs. On the other hand, the transfer function or G_m also shows a dependence with the signal frequency (f_{sig}), as illustrated in Figure 1c, and a non-null imaginary part, introducing frequency response distortion. A detailed characterization of the frequency response is the first step towards the derivation of a complete analytical transfer function to describe the distortions introduced by a non-ideal frequency response in g-SGFETs.

While harmonic distortion is expected to affect more strongly signals of large amplitude, the frequency response is expected to affect more prominently signals with higher frequency components. Due to the wide range of amplitudes and frequencies found in sensing of full-band neural activity, this application is expected to be particularly sensitive to signal distortion. To show the impact of non-ideal response on the sensing capabilities of g-SGFETs, we have measured full-band electrophysiological activity on the rat cortex and in a cell culture. Figure 1d illustrates the effect of distortion on the different signals measured, from large amplitude and low frequency cortical spreading depression events (Figure 1d-top) to high frequency and low amplitude action potentials (Figure 1d-bottom). In order to recover the equivalent signal at the gate (V_{gs-sig}), the measured I_{ds-sig} has to be calibrated by using the inverse of the transfer function. If voltage and frequency dependence of the transfer function, as well as its imaginary part are taken into account, the inverse transfer function will correct the distortions in the output signal, leading to the distortion-free input signal. In order to anticipate changes in the transfer function of the g-SGFET under different conditions and prevent defective calibration, the phenomena involved in signal distortion must be properly understood.

The characterization and modelling of the g-SGFET response reported in this work comprises an important step towards the mitigation of signal distortion in g-SGFETs. On the one hand, the theoretical understanding provided, represents a solid basis for the improvement of the linearity and frequency dependence of the g-SGFET response. On the other hand, the calibration procedure presented represents a method for the acquisition of quasi-distortion-free signals using g-SGFET transducers, with especial potential for the sensing of full-band neural activity.

2. Results and discussion

In this section, the characterization of harmonic distortion and frequency response of g-SGFETs is presented. The measurements have been performed using g-SGFETs on a flexible polyimide substrate (see Experimental Section for details on the fabrication procedure). The devices have been immersed in a phosphate buffered solution (PBS) bath and the gate bias has been applied using an Ag/AgCl reference electrode. The stationary response of the g-SGFETs (I_{ds-DC}) and their dynamic response (I_{ds-sig}) have been characterized under different V_{gs} bias conditions (see Figure 1e). The quasi-DC current and the alternating current signals have been decoupled in order to adapt their dynamic range to fill the full scale of the analog-to-digital converters (see Experimental Section for more details).

2.1. Characterization of harmonic distortion

Harmonic distortion, caused by the voltage dependence of the transfer function in g-SGFET is the result of non-linearities in the I_{ds}-V_{gs} curves. Ideally, GFETs present a particularly linear I_{ds}-V_{gs} relation around their conduction minimum,[21] also referred to as the charge neutrality point (CNP). However, there are various factors that can introduce non-linearities in the response of GFETs.[18] For instance, the resistance between the metal contacts and the graphene channel limits the conductance of the transistor, which can eventually result in a curved I_{ds}-V_{gs} relation away from the CNP. On the other hand, the conductance minimum at the CNP should ideally be perfectly sharp, only limited by thermal fluctuations of charge carriers. However, any inhomogeneous doping of the graphene channel, for instance due to substrate inhomogeneities, can lead to a broadening of the CNP.[22]

Harmonic distortion is commonly characterized by applying test signal and measuring the higher order harmonics generated by signal distortion. In Figure 1c, harmonic distortion is represented in the frequency domain where harmonics at frequencies multiple of f_{sig} can be distinguished. In this section, the harmonic distortion introduced by the g-SGFETs is experimentally determined following this methodology, i.e. applying a pure tone signal at the gate (V_{gs-sig}) and measuring the amplitude of higher order harmonics. Besides, harmonic distortion is also calculated from the Taylor expansion of the stationary $I_{ds} - V_{gs}$ curves. The 0th order term of the Taylor expansion corresponds to the DC current I_{ds-DC} and the 1st order term represents the linear conversion of the signal at the gate. The 2nd and 3rd order terms of the Taylor expansion represent the 2nd and 3rd order harmonics produced by the curvature and

changes in the curvature of the I_{ds} vs V_{gs} curves respectively. Comparing the harmonic distortion levels obtained following these two approaches can be used to validate the stationary description of harmonic distortion, which is critical to correct harmonic distortion in a calibration process.

In **Figure 2**a and 2b this comparison is shown for signals of different amplitudes ($A_{sig} = 2, 4$ and 8 mV_{rms}) in a wide V_{gs} range for a frequency of 10Hz. An excellent agreement between the measured and calculated values is shown for the 1st and 2nd order harmonics in the whole V_{gs} and A_{sig} range. For the 3rd order harmonic this validation is only shown for the $A_{sig} = 8\ mV_{rms}$ due to the contribution from the $1/f$ noise of the g-SGFET, which masks the low amplitude 3rd harmonic for small A_{sig} values (see Figure 2b and Supporting Information S1).

Once we have validated the calculation of harmonic distortion by the Taylor expansion of the $I_{ds} - V_{gs}$ curves, it is possible to calculate the signal-to-distortion ratio (SDR) (i.e. the 1st order harmonic amplitude over the sum of 2nd and 3rd order harmonics) for any combination of A_{sig} and V_{gs} bias conditions(see Figure 2c). The SDR is a figure of merit that can be used to evaluate the impact of distortion on the signal quality. The SDR presents a maximum at $V_{gs} - V_{CNP} \approx \pm 100mV$, where the linearity of the I_{ds}-V_{gs} curve is maximal. The SDR exhibits a minimum close to the CNP due to the abrupt drop of transconductance and the increase of the 2nd order harmonic amplitude. Besides, Figure 2c also reveals that the SDR increases with decreasing A_{sig} values. This dependence is explained by the linear, quadratic and cubic relationship of the 1st, 2nd and 3rd order harmonics, respectively with A_{sig} (see Supporting Information S1). Another useful way to represent the impact of the harmonic distortion on the signal quality is to compare it to the intrinsic $1/f$ noise of the g-SGFET, which is usually considered to limit the signal quality in g-SGFETs.[13,23] Figure 2d shows the distortion-to-noise ratio (DNR) for the noise integrated in a one-decade frequency band (i.e. 4-40Hz). The DNR presents its minimum at $V_{gs} - V_{CNP} \approx \pm 100mV$, its maximum at the CNP and it decreases, as expected, with A_{sig}. The 0dB contour line indicates the parameters for which distortion and noise will contribute with the same power to the degradation of signal quality (see Supporting Information S1 for more details). These results highlight the importance of choosing a right gate bias to minimize the impact of harmonic distortion on the signal quality, especially for large amplitude signals.

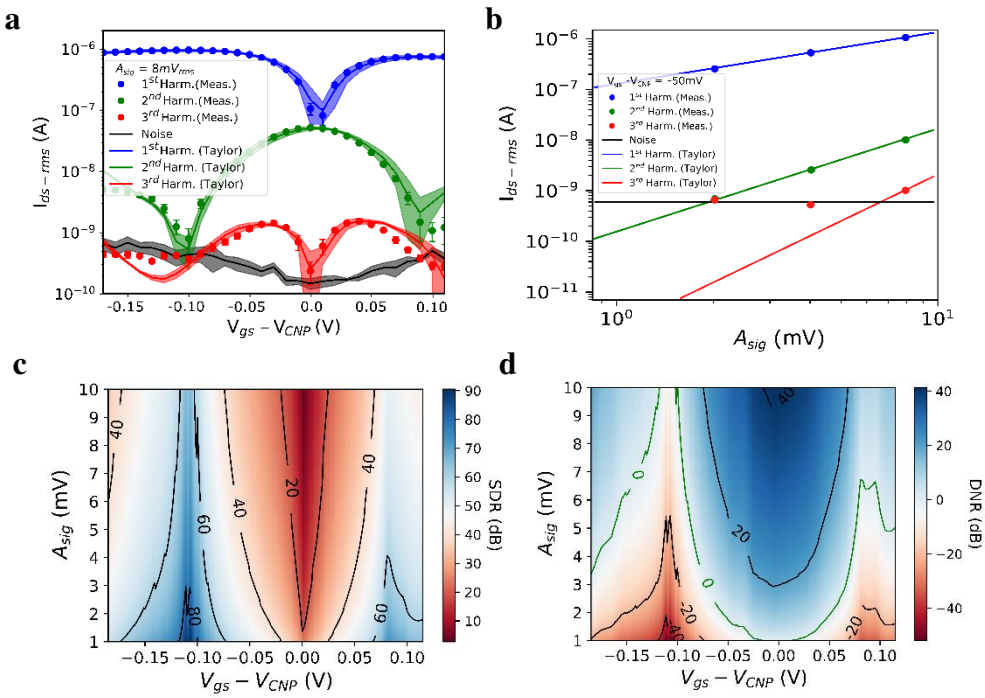

Figure 2: a) 1st, 2nd, and 3rd harmonics rms-amplitude extracted from the power spectrum of the measured I_{ds} (dots) and from the Taylor expansion of the transfer characteristics (solid lines). Error bars and filled areas show the standard deviation (n=4). The noise is evaluated from the power spectrum at 28Hz (i.e. slightly below $3f_{sig}$). The measured and calculated harmonics correspond to a 10Hz signal with an amplitude of 8 mV_{rms}. b) The harmonics obtained experimentally for different signal amplitudes (2, 4 and 8 mV_{rms}) are displayed (dots) together with the calculated values derived from the Taylor expansion. The standard deviation of the measured data with n=4 is smaller than the radius of the dots used to display the data. The data was evaluated at $V_{gs} - V_{CNP} = -0.05V$. c) Evaluation of signal-to-distortion ratio (in dB) in the A_{gs}-V_{gs} parameter map. The solid lines indicate the contour lines of the SDR every 20dBs. d) Distortion-to-noise ratio (in dB) and the contour lines represented by solid lines every 20dBs. The maps in Figure 2c and 2d, are calculated using the Taylor expansion of the stationary $I_{ds} - V_{gs}$ curves.

2.2. Characterization and modelling of the frequency response

In addition to harmonic distortion, non-idealities in the frequency response can also limit the recording capabilities of g-SGFETs. Deviations from a frequency independent transconductance might appear due to for instance a slow charging of the graphene-electrolyte interface capacitance or a slow filling and depletion of trap states in the graphene environment.[24,25] In addition, displacement currents through parasitic capacitances at the graphene-electrolyte interface can also result in the attenuation of the signal.[26] Here, we have characterized the frequency dependence of the magnitude and phase of the g-SGFETs transfer function. The aim of this section is to propose and validate an equivalent circuit and its analytic transfer function, which fully describes the frequency response of the g-SGFETs in a wide range

of signal frequencies and under different experimental conditions. Having such a complete model, a calibration method could be proposed to correct signal distortions introduced by the frequency response of g-SGFETs.

For this purpose, the response of g-SGFETs to input signals ranging from $0.4Hz$ to $200kHz$ has been measured (see Experimental Section for more details). This characterization has been performed for different electrolyte concentrations in order to show the effect that changing the electrolyte (e.g. to physiological medium) could cause on the frequency response. **Figure 3**a shows the experimentally obtained module and phase of the transfer function (Bode diagram) compared with the G_m extracted from the stationary I_{ds}-V_{gs} curves. The Bode diagrams in Figure 3a correspond to the frequency response in a bath with two different ionic concentrations. Apart from the stationary response, they present three regimes of frequency response, each of them represented by a colored region. The $0.4Hz - 3kHz$ range corresponds to a regime characterized by a slight attenuation of the transconductance with an approximately constant slope (in log-scale) and an approximately constant phase deviating few degrees from $180°$ (expected in the holes conduction regime). In the $3kHz - 40kHz$ range, another regime can be observed, in this case only for the low ionic concentration experiment, which consists of an abrupt attenuation of the gain with frequency ($\sim 1/f$). The attenuation in magnitude goes along with a negative shift of the phase. Finally, a high frequency regime (above $40kHz$) is characterized by an increase of both the magnitude and phase of the transconductance.

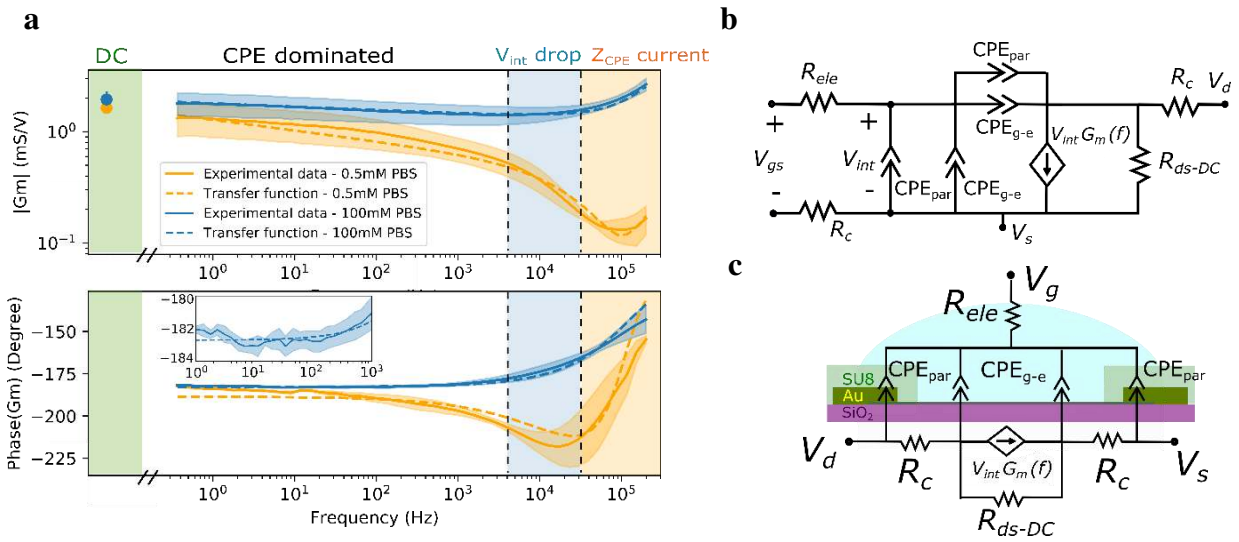

Figure 3: a) Bode diagram of g-SGFETs (n=4). Three different response regimes are displayed together with the G_m extracted from the DC characteristics: CPE dominated regime, a regime where the G_m drops with approximately $1/f$ and finally a G_m increase due to capacitive currents **b.** Small signal model of the g-SGFET frequency response. The gate-to-source bias bias (V_{gs}) and the drain voltage (V_d) are defined. The voltage drop at the graphene-electrolyte interface is defined as V_{int}. The CPE_{g-e} represents the constant phase element (CPE) describing the non-ideal capacitive behavior of the graphene-electrolyte interface. The CPE describing the leakage through parasitic elements is defined as CPE_{par}. The resistance of the electrolyte (R_{ele}) and the contact resistance of the g-SGFET (R_c) are defined. The dynamic response of the g-SGFET is modelled by the current source ($V_{int}G_m(f)$) and its stationary response is modelled by the resistance in parallel R_{ds-DC}. c) The equivalent circuit shown in c. is drawn on a schematic of the g-SGFET to illustrate the physical origin of each element.

Having identified these three regimes of frequency response, it is now possible to propose a small signal model of the g-SGFET (see Figure 3b and 3c). In the proposed equivalent circuit, the graphene-electrolyte interface is not modelled as an ideal capacitor, as done in standard models,[18] but instead as a constant phase element (CPE_{g-e}) which is commonly required to properly describe the response of a double-layer capacitance.[27,28] Although CPEs are often used in electrochemical impedance modelling, its physical origin is still a topic under discussion.[29,30] In the particular case of the graphene-electrolyte interface it has been previously reported in impedance measurements[28]. The equivalent circuit in Figure 3b and 3c also includes the resistance of the electrolyte R_{ele} and the contacts R_c in series with the graphene-electrolyte interface. The V_{gs} applied causes a voltage drop at the graphene-electrolyte interface (V_{int}) which is transduced by the g-SGFET. The conversion of AC signals at the gate is modelled by a current source element $V_{int}G_m(f)$ while the DC current flowing through the g-SGFET is modelled by the element R_{ds-DC}. Finally, an additional CPE, CPE_{par}, is added in parallel with CPE_{g-e} to account for parasitic capacitances in the device. Possible

parasitic elements might originate in a capacitive coupling of the electrolyte with the metal lines in the device, caused by an excessively thin or defective passivation of the metal lines. Using this equivalent circuit, we can derive an analytic expression which describes the frequency dependent transfer function of the g-SGFET.

$$G_m(f) = \left.\frac{dI_{ds}}{dV_{int}}\right|_{V_{ds}} \frac{dV_{int}}{dV_{gs}} + G_{m,eff} \quad (1)$$

The first factor on the right hand side of **Equation (1)** corresponds to the intrinsic transconductance, and it presents a frequency dependence that results from the non-ideal capacitive behavior of the interface,[31] i.e. $dI_{ds}/dV_{int}|_{V_{ds}} = kC_{CPE_{g-e}}(f)$ (see Supporting Information S2 for more details). The second factor in Equation (1) results from the contribution of the resistance in series (R_s) with the g-SGFET (i.e. R_c plus R_{ele}) andCPE_{par} in parallel with the transistor, which are responsible for the attenuation of the signal at the interface V_{int} with frequency [18] (see Supporting Information S2 and S3). The last term in Equation (1) has to be included to account for the measured increase of the transconductance at high frequencies. When a signal is applied at the gate, the CPE_{g-e} and CPE_{par} elements represent a direct current path between gate and the g-SGFET contacts. The impedance of these CPE elements characterizes this capacitive current, which adds-up to the drain-to-source current. This contribution is not result of the field-effect coupling, and can be therefore regarded as an effective transconductance ($G_{m_{eff}}$) term. Above a certain frequency, this capacitive contribution to the current measured at the drain is expected to dominate the frequency response, as shown in Figure 3a. The frequency dependence of the terms in Equation (1) can be expressed explicitly as shown in the Supporting Information S2.

Figure 3a shows the fitting of the experimentally obtained frequency response (magnitude and phase) with the transfer function derived using the equivalent circuit of Figure 3b (fitting parameters can be found in the Supporting Information S2). All the main features of the frequency response described previously are properly captured. The close match between experimental data and the derived $G_m(f)$ validates the proposed equivalent circuit. The understanding of the frequency response provided by this model represents a strong basis for future improvements of the g-SGFET response (see Supporting Information S4). Furthermore, the derived transfer function can be used to set a calibration procedure to cancel signal distortions introduced by the non-ideal frequency response of the g-SGFETs.

2.3. Calibration of harmonic distortion using the non-linear stationary I_{ds}-V_{gs} curve

We have previously discussed that harmonic distortion can degrade the signal quality significantly, especially for signals with large amplitudes and for not optimum gate bias conditions. Under these conditions, correction of the harmonic distortion by a proper calibration methodology can be critical. The conversion of measured signals in current (I_{ds-sig}) back to an equivalent voltage at the gate (V_{gs-sig}) is commonly done using a constant factor, i.e. the voltage-independent G_m of the GFETs, which is estimated at the bias point of operation. However, following this approach harmonic distortion is rescaled together with the original signal, but not corrected. In order to correct harmonic distortion we propose to interpolate the measured I_{ds-sig} into the $I_{ds} - V_{gs}$ curves (see Supporting Information S5).

In order to validate this calibration procedure, which takes into account the voltage dependence of G_m, we have quantified the attenuation of the 2nd harmonic after calibration. **Figure 4**a shows the 2nd harmonic of a pure tone signal applied at the gate after calibration using a constant G_m or by interpolating into the $I_{ds} - V_{gs}$ curves. Using the interpolation method, we can obtain a very effective attenuation of the distortion; confirmed by the observation that the 2nd harmonic drops to values very close to the noise level (black line). Yet, the amplitude of the second order harmonic increases significantly around the CNP due to the loss of transconductance and inaccuracies in the determination of the $I_{ds} - V_{gs}$ curves. Another possible source of deviation from an ideal correction of harmonic distortion is the frequency dependence of G_m (see Supporting Information S6).

In order to show the impact of harmonic distortion on relevant electrophysiologic data, CSD events have been recorded in a headfixed rat model (see Experimental Section and reference [15]). These signals are specially prone to harmonic distortion because of their large amplitude. Figure 4b shows the electrophysiological signal recorded using a g-SGFET for a $V_{gs} - V_{CNP} = -0.04V$ and subsequently calibrated using a constant G_m (black line) or by interpolation of the signal into the $I_{ds} - V_{gs}$ curves (orange line). The results show that harmonic distortion modifies the amplitude of the CSD signals, reaching changes of $\sim 1.5mV$ (i.e. $\sim 10\%$ of the total amplitude) in a V_{gs} range where g-SGFETs present an otherwise proper performace (see Supporting Information S5 for more details).

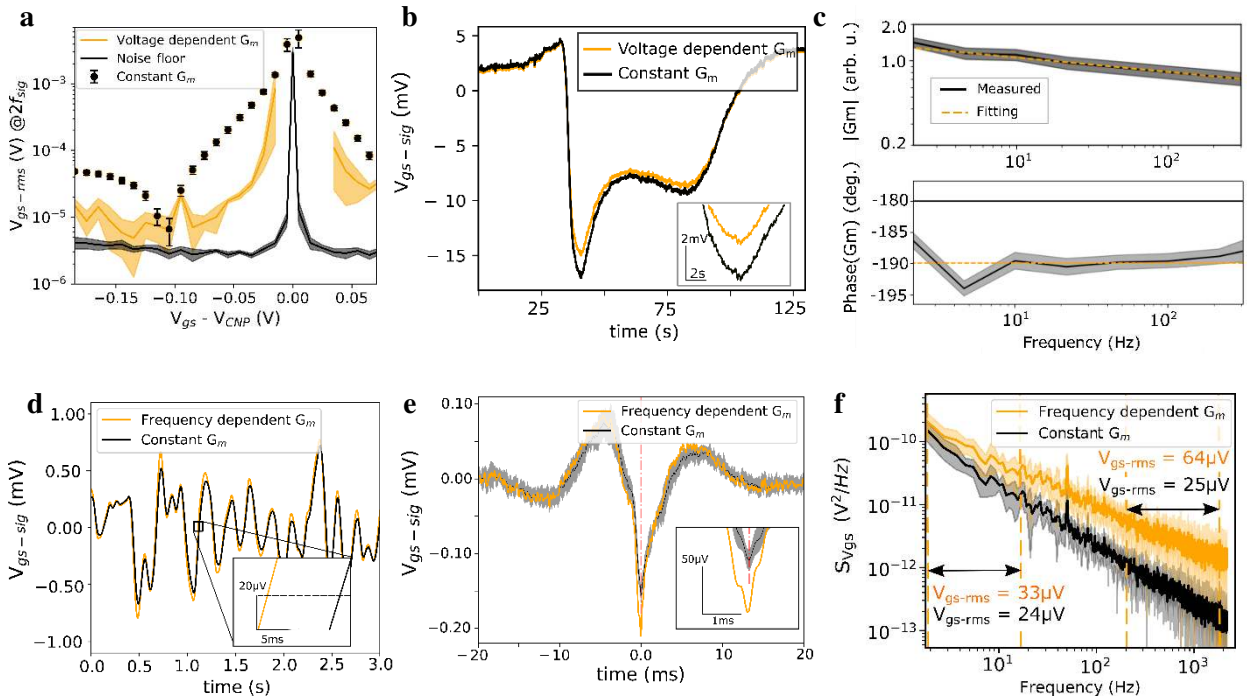

Figure 4: a) Amplitude of the second harmonic in the equivalent voltage at the gate for $A_{sig} = 8mV_{rms}$, showing the values calibrated using a constant transconductance (dots) and using the interpolation into the transfer characteristics (solid orang line). The solid black line shows the average intrinsic noise of the g-SGFET measured at 17Hz and 23Hz (i.e. 3Hz below and above $2f_{sig}$). The errorbars and filled area show the standard deviation for n=4. b) A cortical spreading depression signal (CSD) recorded from the cortex of a rat calibrated with the non-linear transfer characteristics and distorted according to static non-linearities far and close to the CNP. c) Frequency response measured *in-vivo* of the g-SGFETs used for the recording of LFP signals. The filled area shows the standard deviation (n=4) and the orange dashed line the fitting using the derived transfer function (α = 0.88). d) A LFP signal recorded from the cortex of a rat (see Experimental Section) is shown in the 1-10Hz bandwidth. The signal calibrated using a constant G_m is shown in black while the signal calibrated using the derived transfer function is plotted in orange. e) Average of 15 action potentials recorded from a HL-1 cardiomyocyte. The filled area shows the standard deviation and the orange line the calibrated signal using the derived TF. The frequency response for this devices is shown in the Supporting Information S4. f) PSD of the equivalent voltage noise at the gate obtained from calibrating with a constant G_m (black) or interpolating into the transfer characteristics (orange). The V_{gs-rms} indicates the rms of the PSD withing the dashed vertical lines.

2.4. Calibration of LFP activity and APs using the inverse transfer function

The dependence of G_m on the non-ideal double layer capacitance of the graphene-electrolyte interface makes the response of the g-SGFETs to change with frequency even at low frequencies. Small deviations from ideality can cause relatively large changes in the G_m amplitude and phase. Signals showing a wide band activity such as local field potentials, with frequency components ranging from $\sim 1Hz$ to $\sim 200Hz$,[32,33] will present a more pronounced distortion of the signal shape produced by different amplification of various frequency

components. In addition, phase distortion might cause defective phase determination in LFPs.[19] To show the impact of non-ideal frequency response on actual physiologic data, LFPs have been recorded *in-vivo* on the rat cortex using epicortical g-SGFET flexible probes (see Experimental Section) and action potentials have been recorded from a HL-1 cell culture on a g-SGFET array fabricated on a SiO_2 rigid substrate (see Experimental Section).

In order to calibrate the electrophysiological data, the frequency response of the g-SGFETs under *in-vivo* conditions and in the culture medium must be known. Figure 4c shows the frequency response of the g-SGFETs measured on the rat cortex (see Experimental Section), while the response of the g-SGFETs in the culture medium is shown in Supporting Information S4. In the frequency range relevant for the recording of LFPs and APs, the Bode plots show a frequency response dominated by the CPE behaviour described previously. In this regime, the $G_m(f)$ can be approximated by $G_m(f = 1Hz)\ /f^{1-\alpha}$ (see fitting in Figure 4c and the Supporting Information S7 for a description of the numerical implementation of the frequency dependent transfer function).

The impact of such distortions can be shown by calibrating the recorded signals using the inverse of the fitted $G_m(f)$. Figure 4d shows a LFP signal in the (1-10Hz frequency band) calibrated using a frequency independent G_m and using the frequency dependent transfer function of the g-SGFETs in the *in-vivo* conditions. The non-ideal frequency response causes changes in the signal amplitude as well as phase shifts of ~ 10 degrees. Similarly, Figure 4e shows an average of 15 action potentials recorded in an *in-vitro* cardiomyocyte culture. In the case of the APs, neglecting the effect of frequency response leads to a significant error in the amplitude determination (an understimation of $\sim 30\%$ of the actual amplitude) due to the high frequency of these signals.

Finally, G_m loss at high frequencies will cause loss of signal-to-noise ratio that cannot be corrected by calibration. Figure 4f shows the effect of G_m loss on the power spectral density (PSD) of the calibrated noise ($S_{V_{gs}}$). The understimation in the noise power made by using a constant G_m for calibration can be quantified by integrating the PSD in different frequency bandwidths (see Figure 4f), leading to different values of equivalent noise at the gate (V_{gs-rms}).

These results emphasize the importance of understanding and improving the frequency response of g-SGFETs, especially for sensing high frequency and low amplitude signals. It is also shown the importance of characterizing the frequency response of the g-SGFETs in the

environment used for the final application, in our case on the brain cortex, for a proper calibration of the signal.

3. Conclusion

In summary, this work provides a detailed characterization and modelling of the signal distortion mechanisms in g-SGFETs, describing their impact on the recording capabilities of these devices. The effect of distortion on electrophysiological signals has been evaluated in a wide frequency and amplitude range. It has been shown that non-linearities in the $I_{ds} - V_{gs}$ curves can have a significant impact on the amplitude and shape determination of large amplitude signals, such as spreading depression events. This distortion can be corrected by a calibration procedure which takes into account the voltage dependence of G_m. On the other hand, the non-ideal frequency response of g-SGFETs results in a significant effect on the amplitude determination of LFPs and APs as well as on the phase extraction for LFPs. These distortions can be calibrated using the frequency dependent transfer function presented in this work, following a similar approach as previously proposed for microelectrodes when a frequency independent gain cannot be obtained.[19]

In spite of performing a proper calibration of the signal, conventional microelectrodes introduce dramatic SNR loss at infra-slow frequencies.[19] Alternatively, g-SGFETs present a high G_m at low frequencies, allowing to record infra-slow neural activity with a high sensitivity. This high G_m slightly drops as the frequency is increased, therefore producing a progressive loss of SNR. Eliminating the frequency dependence of G_m is thus a clear strategy towards improving the already outstanding sensitivity of g-SGFETs at high frequencies. The understanding of the g-SGFET response provided in this work sets the ground to their frequency response as well as to mitigate harmonic distortion by operating the devices at optimum bias conditions. Finally, and more importantly, the calibration procedures presented in this work have been shown effective to correct the impact of signal distortion on the recording capabilities of g-SGFETs. These results demonstrate the potential of g-SGFETs as a highly sensitive, distortion-free platform, not only for full-band neural sensing, but also for a broader range of applications in which g-SGFET sensors are used.

4. Experimental Section

Fabrication of g-SGFETs: Arrays of g-SGFETs were fabricated on a 10 µm thick polyimide (PI-2611, HD MicroSystems) film spin coated on a Si/SiO_2 4" wafer and baked at $350°C$. A first metal layer (10nm Ti/100nm Au) was deposited by electron-beam vapour and then structured by a lift-off process. Afterwards, the graphene grown by chemical vapour deposition on Cu was transferred (process done by Graphenea s.a.). Graphene was then patterned by oxygen plasma (50 sccm, 300W for 1min) in a reactive ion etching (RIE) after protecting the graphene in the channel region with HIPR 6512 (FujiFilm) positive photoresist. After the graphene etching, a second metal layer was patterned on the contacts following the same procedure as for the first layer. The lift-off was followed by an annealing in ultra-high vacuum consisting on a temperature ramp from room temperature to 300°C. Subsequently, the transistors were insulated with a 3-µm-thick photodefinable SU-8 epoxy photoresist (SU-8 2005 Microchem), keeping uncovered the active area of the transistors channel and the contacting pads. The polyimide substrate was structured in a reactive ion etching process using a thick AZ9260 positive photoresist (Clariant) layer as an etching mask. The neural probes were then peeled off from the wafer and placed in a zero insertion force connector to be interfaced with our custom electronic instrumentation. Finally, the devices were rinsed for 2 minutes in ethanol to eliminate remaining resist residues on the graphene channel.

Electrical characterization in PBS: To measure the DC and AC accurately, the electrical current from drain to source is pre-amplified in a first amplification stage with a "low" 10^4 gain. The pre-amplified signal is then low-pass filtered and subtracted from the pre-amplified signal, thus canceling its low frequency (i.e. DC level) components. The resulting signal can therefore be further amplified and low-pass (anti-aliasing) filtered in a second stage with an additional 10^2 gain factor. A custom built circuit was used for the amplification of the current signals, which were digitalized using a NI DAQCard in all characterization procedures *in-vitro*. For the characterization of harmonic distortion, the DC and AC components of the signal were measured. The 1st, 2nd and 3rd order harmonics of a 10Hz signal applied at the gate were determined from the output of the second amplification stage while the stationary $I_{ds} - V_{gs}$ curves used to calculate harmonic distortion were obtained from the first amplification stage.
The frequency response was characterized by applying a composed signal on the electrolyte containing the superposition of sine waves (12 frequencies per decade with an amplitude of 1mVpk) in the bandwidth of interest (i.e. 0.4Hz-200kHz). Different concentrations of PBS (0.05X and 10X) were used in order to assess the effect of the electrolyte conductivity on the frequency response, where the composition of PBS 1X is 10mM Na_2HPO_4, 1.8mM KH_2PO_4,

2.7mM KCl and 137mM NaCl. The signal from the first amplification stage was used to have access to a wider frequency bandwidth (from 0.35Hz to 200kHz).

Ethical approval and animal handling: All experimental procedures were conducted in accordance with the European Union guidelines on protection of vertebrates used for experimentation (Directive 2010/63/EU of the European Parliament and of the Council of 22 September 2010). The experiments for the recording of CSD events were approved by the ethics committee of the Hospital Clinic de Barcelona. Rats were kept under standard conditions (room temperature 23 ± 1 °C, 12:12 h light–dark cycle, lights on at 08:00), with food (A04, Harlan) and water available ad libitum. Experiments for the recording of LFP were in accordance with the German Law for Protection of Animals (TierSchG), and were approved by the local authorities (ROB-55.2-2532.Vet_02-16-170). Rats were kept under standard conditions (room temperature 22 ± 2 °C, 12:12 h light–dark cycle, lights on at 10:00), with food (V1534-000, SSNIFF) and water available ad libitum.

Recording of CSD events in a rat model and calibration of harmonic distortion: The procedure followed has been thoroughly described previously[15]. The data from one of the rats used in this previous study has been used for evaluating the effect of harmonic distortion on infra-slow CSD signals.

The adult Wistar rats used for this study were deeply anaesthetized with isoflurane (4% induction, 1-3% maintenance) and all pressure and incision points were infiltrated with local anaesthetic lidocaine. A craniotomy was performed on the left hemisphere (centred at 43 mm anterio-posterior (AP) and 42.5 mm medio-lateral (ML) and was 6 mm AP by 4.5 mm ML in size). An additional craniotomy was performed on the prefrontal cortex to administer 5mM KCl to induce CSD events. A Ag/AgCl electrode pellet was inserted in temporal muscle and used as reference both for recordings and for the measurement of the transistor transfer curve.

The DC signals from the first amplification stage and bias control were managed by a data acquisition system (National Instruments USB-6353). On the other hand, the AC signals from the second amplification stage were directly acquired by a commercial electrophysiological recording system consisting of a programmable gain amplifier (Multichannel Systems) and digitizer interface (CED 1401 and Spike2 software, Cambridge Electronic Design). The DC and AC bands were sampled at 1 Hz and 5 kHz respectively. Before the beginning of the recordings, the transfer curve of the g-SGFET was measured in situ.

Recording of LFP activity on the rat cortex: An adult Long Evans rat was used for the measurement of local-field potential signals in this study. The rat, weighing 580 g, was deeply anaesthetized with MMF (Midazolam 2mg/kg, Medetomidin 0.15 mg/kg, Fentanyl 0.005

mg/kg). Starting 1h after MMF induction Isoflurane was supplemented for maintenance at 1% and Metamizol was given at 110 mg/kg. The posterior-dorsal area of the head was shaved, the skin locally desinfected with Povidone-iodine and subcutaneously infiltrated with local anasthetic Bupivacaine. Subsequently the skin was incised and the dorsal skull cleaned carefully by blunt dissection. The dried skull was covered with UV-curing adhesive Optibond (Kerr) and a 3D printed base ring was anchored to skull with screws and Metabond cement (Parkell).

Symmetric craniotomies with a maximum width of 5 mm were performed bilaterally, extending between +2 mm and -8mm with respect to bregma in the anterior-posterior axis.

The dura mater was incised and removed within these craniotomies. A further craniotomy of 1x1 mm was performed over the cerebellum. All craniotomies were covered with prepolymerized PDMS (Sylgard 184, Dow Corning, USA) with mixing ratio 1:10 and sealed with Vetbond (Animal Care Products, USA). The skin margins around the implant were sutured and the implant closed with a protective cap.

After 1 week of recovery the g-SGFET array was implanted under Isofluran Anesthesia (5% induction 1% maintenance). After partial opening and sidewards flapping of the polymer covering the right hemisphere the array was placed onto the pial surface positioned such as to cover the posterior aspect of the right hemisphere (ca -7 to -2 mm from bregma). In addition two Pt-Ir wires were implanted at either side of the g-SGFET array. One proximal to the array, the other distally on the opposing hemisphere. The polymer cover was flapped back into position with the flexible cable of the g-SGFET array leaving through the remaining slit. A second PDMS cover was used to cover both the incised polymer and array, anchored to the skull with Vetbond and Evoflow (Ivoclar Vivadent, Liechtenstein) and sealed with silicon gel 3-4680 (Dow Corning, USA).

An Ag/AgCl electrode was placed in contact with the cerebellum as a reference for the recording of LFP as well as the - curves and frequency response for calibration of the neural signals.

The recordings were performed using a custom built data acquisition system with capabilities to switch between the output of the 1st and the 2nd amplification stages. The former was used for the acquisition of LFP activity while the latter was used for the determination of the curves needed for calibration.

Characterization of frequency response in-vivo for calibration of LFP: The frequency response of the g-SGFETs has been observed to depend on the ion concentration in the

electrolyte. For this reason, the frequency response has to be properly determined *in-vivo* for subsequent calibration of detected neural activity.

To obtain the frequency response *in-vivo*, two Pt-Ir wires were implanted at either side of the g-SGFET array. The two Pt-Ir wires were then connected to a current signal generator to perform a bipolar current stimulation at different frequencies. The current signal generator was decoupled from the recording system in order to avoid any current to leak through the g-SGFETs. The amplitude of the current signal was $1\mu A$ which is small for causing ephaptic effects. The amplitude of stimulation was decreased by a 2-fold to validate that the measured G_m dropped by the same factor. The signal was applied in current to avoid any effect of the electrode and tissue impedances on the amplitude of the signal at different frequencies. By imposing a current, the amplitude in volts at the g-SGFETs site is expected to be constant with frequency. The drawback of this approach is that the amplitude in volts of the signal applied is not known and therefore the extracted magnitude of the Bode must be expressed in arbitrary units.

The parameters of the analytic transfer function which describe the frequency response can be obtained by fitting the Bode plot. The only parameter that cannot be obtained from this fitting is the scaling factor or transconductance at $f = 1Hz$. However, this parameter can be obtained from the first derivative of the static $I_{ds} - V_{gs}$ curves with small uncertainty as shown in Figure 3a. Having all the extracted parameters, it is possible to define the inverse $G_m(f)$, which can be then used to calibrate the data recorded *in-vivo*.

*Culture of HL-1 cardiomyocytes and recording of action potentials: T*he HL-1 cell line was obtained from the LSU Health Sciences Center New Orleans, USA. Cells were culture on Claycomb medium supplemented with 10% FBS, Penicillin/Streptomycin (100 U/ml:100 µg/ml) and L-Glutamine (2mM) on a flask coated with fibronectin/gelatin and incubated at 37ºC with 5 % CO2. The culture medium was exchanged daily and supplemented with fresh Norepinephrine 0.1 mM. When the cells were beating, they were subcultured on new flask or on the g-SGFET arrays as needed. To do so, cells were detached from the flask using trypsin and after a few minutes' incubation at 37ºC the enzymatic activity was neutralized using twice the volume of culture media. The solution containing the cells was centrifuged at 120 g for 2 minutes and the supernatant was aspired before re-suspending the cells on fresh culture media. The cells were seeded then on the desired substrate. To prepare them for culture, the g-SGFET were sterilized in 70% ethanol for 15 minutes, rinsed several times with PBS and coated with fibronectin/gelatine for at least 2 hours. Then the fibronectin/gelatine was aspired and the device was rinsed again with PBS. Experiments were performed 48 to 72 hours after subculture.

All chemicals are bought from Sigma Aldrich unless otherwise noted. The action potentials recording was performed using the home-built system schematized in Figure 1e and described before. The signals were digitalized from the second amplification (band-pass filtered) stage. The transistors were operated at a constant source-drain and gate voltage. Signals were recorded at a sampling frequency of Fs = 20 kHz and digitally band-pass filtered from 55 Hz to 4 kHz after digitalization. The same setup used for the characterisation of the g-SGFETs in a PBS bath was used for the recording of electrophysiological signals from the cell culture. The output from the 1st amplification stage was used for the determination of the transfer characteristics while the output from the 2nd stage was used for the recording of recording of action potentials. The frequency response was determined following the same approach as for its characterization in a PBS bath.

Supporting Information

Supporting Information is available from the Wiley Online Library or from the author.

Acknowledgements

This work has been funded by the European Union's Horizon 2020 research and innovation programme under Grant Agreement No 696656 (Graphene Flagship) and Grant Agreement No. 732032 (BrainCom). The ICN2 is supported by the Severo Ochoa Centres of Excellence programme, funded by the Spanish Research Agency (AEI, grant no. SEV-2017-0706), and by the CERCA Programme / Generalitat de Catalunya. The co-author Ramon Garcia-Cortadella is supported by the International PhD Programme La Caixa - Severo Ochoa (Programa Internacional de Becas "la Caixa"-Severo Ochoa). This work has made use of the Spanish ICTS Network MICRONANOFABS partially supported by MICINN and the ICTS 'NANBIOSIS', more specifically by the Micro-NanoTechnology Unit of the CIBER in Bioengineering, Biomaterials and Nanomedicine (CIBER-BBN) at the IMB-CNM.

Received: ((will be filled in by the editorial staff))
Revised: ((will be filled in by the editorial staff))
Published online: ((will be filled in by the editorial staff))

References

[1] L. Banszerus, M. Schmitz, S. Engels, J. Dauber, M. Oellers, F. Haupt, K. Watanabe, T. Taniguchi, B. Beschoten, C. Stampfer, *Sci. Adv.* **2015**, *1*, e1500222.

[2] F. Banhart, J. Kotakoski, A. V. Krasheninnikov, *ACS Nano* **2011**, *5*, 26.

[3] B. R. Goldsmith, L. Locascio, Y. Gao, M. Lerner, A. Walker, J. Lerner, J. Kyaw, A. Shue, S. Afsahi, D. Pan, J. Nokes, F. Barron, *Sci. Rep.* **2019**, *9*, 434.

[4] J. Peña-Bahamonde, H. N. Nguyen, S. K. Fanourakis, D. F. Rodrigues, *J. Nanobiotechnology* **2018**, *16*, 75.
[5] R. Hajian, S. Balderston, T. Tran, T. deBoer, J. Etienne, M. Sandhu, N. A. Wauford, J.-Y. Chung, J. Nokes, M. Athaiya, J. Paredes, R. Peytavi, B. Goldsmith, N. Murthy, I. M. Conboy, K. Aran, *Nat. Biomed. Eng.* **2019**, *3*, 427.
[6] W. Tian, X. Liu, W. Yu, W. Tian, X. Liu, W. Yu, *Appl. Sci.* **2018**, *8*, 1118.
[7] W. Yuan, G. Shi, *J. Mater. Chem. A* **2013**, *1*, 10078.
[8] Y. Zhu, C. Wang, N. Petrone, J. Yu, C. Nuckolls, J. Hone, Q. Lin, in *2015 28th IEEE Int. Conf. Micro Electro Mech. Syst.*, IEEE, **2015**, pp. 869–872.
[9] B. Mailly-Giacchetti, A. Hsu, H. Wang, V. Vinciguerra, F. Pappalardo, L. Occhipinti, E. Guidetti, S. Coffa, J. Kong, T. Palacios, *J. Appl. Phys.* **2013**, *114*, 084505.
[10] K. Maehashi, Y. Sofue, S. Okamoto, Y. Ohno, K. Inoue, K. Matsumoto, *Sensors Actuators B Chem.* **2013**, *187*, 45.
[11] K. Kostarelos, M. Vincent, C. Hebert, J. A. Garrido, *Adv. Mater.* **2017**, *29*, 1700909.
[12] B. M. Blaschke, N. Tort-Colet, A. Guimerà-Brunet, J. Weinert, L. Rousseau, A. Heimann, S. Drieschner, O. Kempski, R. Villa, M. V Sanchez-Vives, J. A. Garrido, *2D Mater.* **2017**, *4*, 025040.
[13] C. Hébert, E. Masvidal-Codina, A. Suarez-Perez, A. B. Calia, G. Piret, R. Garcia-Cortadella, X. Illa, E. Del Corro Garcia, J. M. De la Cruz Sanchez, D. V. Casals, E. Prats-Alfonso, J. Bousquet, P. Godignon, B. Yvert, R. Villa, M. V. Sanchez-Vives, A. Guimerà-Brunet, J. A. Garrido, *Adv. Funct. Mater.* **2018**, *28*, 1703976.
[14] E. J. W. van Someren, *Slow Brain Oscillations of Sleep, Resting State and Vigilance : Proceedings of the 26th International Summer School of Brain Research, Held at the Royal Netherlands Academy of Arts and Sciences, Amsterdam, the Netherlands, 29 June-2 July, 2010*, **n.d.**
[15] E. Masvidal-Codina, X. Illa, M. Dasilva, A. B. Calia, T. Dragojević, E. E. Vidal-Rosas, E. Prats-Alfonso, J. Martínez-Aguilar, J. M. De la Cruz, R. Garcia-Cortadella, P. Godignon, G. Rius, A. Camassa, E. Del Corro, J. Bousquet, C. Hébert, T. Durduran, R. Villa, M. V. Sanchez-Vives, J. A. Garrido, A. Guimerà-Brunet, *Nat. Mater.* **2019**, *18*, 280.
[16] S. Drieschner, A. Guimerà, R. G. Cortadella, D. Viana, E. Makrygiannis, B. M. Blaschke, J. Vieten, J. A. Garrido, *J. Phys. D. Appl. Phys.* **2017**, *50*, 095304.
[17] M. D. Stoller, C. W. Magnuson, Y. Zhu, S. Murali, J. W. Suk, R. Piner, R. S. Ruoff, *Energy Environ. Sci.* **2011**, *4*, 4685.
[18] C. Mackin, L. H. Hess, A. Hsu, Y. Song, J. Kong, J. A. Garrido, T. Palacios, *IEEE Trans. Electron Devices* **2014**, *61*, 3971.
[19] M. J. Nelson, P. Pouget, E. A. Nilsen, C. D. Patten, J. D. Schall, *J. Neurosci. Methods* **2008**, *169*, 141.
[20] S. Rodriguez, A. Smith, S. Vaziri, M. Ostling, M. C. Lemme, A. Rusu, **2014**, DOI 10.1109/TED.2014.2326887.
[21] K. A. Jenkins, D. B. Farmer, S.-J. Han, C. Dimitrakopoulos, S. Oida, A. Valdes-Garcia, *Appl. Phys. Lett.* **2013**, *103*, 173115.
[22] S. Samaddar, I. Yudhistira, S. Adam, H. Courtois, C. B. Winkelmann, *Phys. Rev. Lett.* **2016**, *116*, 126804.
[23] I. Heller, S. Chatoor, J. Männik, M. A. G. Zevenbergen, J. B. Oostinga, A. F. Morpurgo, C. Dekker, S. G. Lemay, **2010**, *10*, 1563.
[24] M. Winters, E. Ö. Sveinbjörnsson, N. Rorsman, *J. Appl. Phys.* **2015**, *117*, 074501.
[25] H. Wang, Y. Wu, C. Cong, J. Shang, T. Yu, *ACS Nano* **2010**, *4*, 7221.
[26] C. Mackin, E. McVay, T. Palacios, C. Mackin, E. McVay, T. Palacios, *Sensors* **2018**, *18*,

494.
[27] E. Barsoukov, J. R. Macdonald, Eds. , *Impedance Spectroscopy*, John Wiley & Sons, Inc., Hoboken, NJ, USA, **2005**.
[28] J. Sun, Y. Liu, *Nanomaterials* **2019**, *9*, 923.
[29] C.-H. Kim, S.-I. Pyun, J.-H. Kim, *Electrochim. Acta* **2003**, *48*, 3455.
[30] W. H. Mulder, J. H. Sluyters, T. Pajkossy, L. Nyikos, *J. Electroanal. Chem. Interfacial Electrochem.* **1990**, *285*, 103.
[31] C. H. Hsu, F. Mansfeld, *CORROSION* **2001**, *57*, 747.
[32] G. Buzsáki, B. O. Watson, *Dialogues Clin. Neurosci.* **2012**, *14*, 345.
[33] G. Buzsáki, C. A. Anastassiou, C. Koch, *Nat. Rev. Neurosci.* **2012**, *13*, 407.

Table of contents: **Distortion-free sensing using active graphene sensors has been enabled for a wide frequency bandwidth and a large range of signal amplitudes.** The voltage and frequency dependence of the sensors gain has been thoroughly characterized and modelled leading to a complete transfer function, which can be used for calibration of the detected signals with unprecedented accuracy.

Keyword: harmonic distortion, frequency response, graphene, solution-gated, neural sensing

*Ramon Garcia-Cortadella, Eduard Masvidal-Codina, Jose de la Cruz, Nathan Schäfer, Gerrit Schwesig, Christoph Jeschke, Javier Martinez-Aguilar, Maria V. Sanchez-Vives, Rosa Villa, Xavi Illa, Anton Sirota, Anton Guimerà and Jose A. Garrido**

Distortion-Free Sensing of Neural Activity Using Graphene Transistors

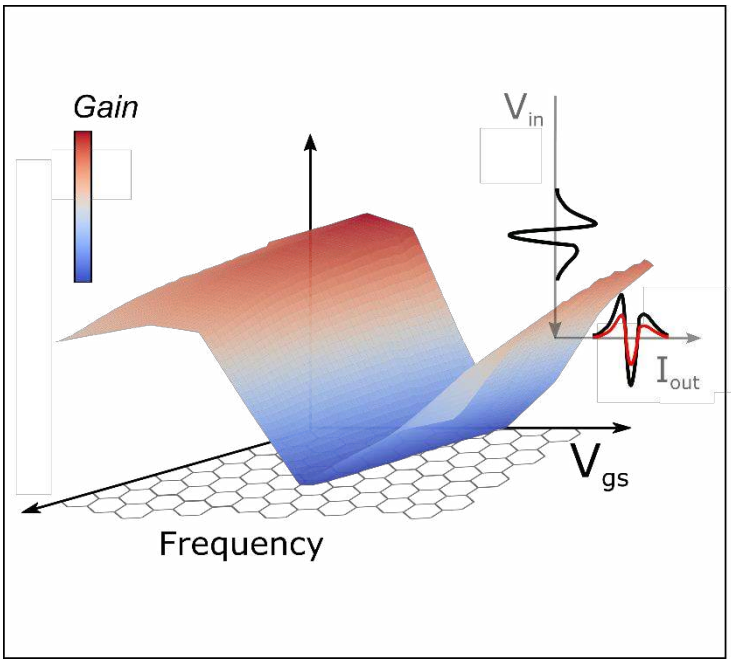

Copyright WILEY-VCH Verlag GmbH & Co. KGaA, 69469 Weinheim, Germany, 2016.

Supporting Information

Distortion-Free Sensing of Neural Activity Using Graphene Transistors

*Ramon Garcia-Cortadella, Eduard Masvidal-Codina, Jose de la Cruz, Nathan Schäfer, Gerrit Schwesig, Christoph Jeschke, Javier Martinez-Aguilar, Maria V. Sanchez-Vives, Rosa Villa, Xavi Illa, Anton Sirota, Anton Guimerà and Jose A. Garrido**

S1. Comparison of calculated harmonic distortion with experimental data

As mentioned in the introduction of the main text, harmonic distortion introduced by the GFETs can, in principle, be calculated from the Taylor expansion of the $I_{ds} - V_{gs}$ curves (**Equation (S1)**). The expansion to the 3rd order can be expressed as follows:

$$I_{ds} = I_{ds}|_{V_{gs}o} + \left.\frac{dI_{ds}}{dV_{gs}}\right|_{V_{gs}o} A_{sig}\sin(2\pi f t) + \frac{1}{2!}\left.\frac{d^2 I_{ds}}{d{V_{gs}}^2}\right|_{V_{gs}o} \frac{{A_{sig}}^2}{2}\sin(4\pi f t) + \frac{1}{3!}\left.\frac{d^3 I_{ds}}{d{V_{gs}}^3}\right|_{V_{gs}o} \frac{{A_{gsig}}^3}{4}\sin(6\pi f t) \tag{S1}$$

where A_{sig} represents the amplitude of the small signal applied at the gate V_{gs-sig} (see Figure 1b) in the main text.

Figure 2a in the main text shows the agreement between measured harmonic distortion and the values calculated from the stationary $I_{ds} - V_{gs}$ curves for a signal amplitude $A_{sig} = 8mV_{rms}$. Here the agreement for the other measured signal amplitudes ($A_{sig} = 4$ and $2\ mV_{rms}$) is also shown for a wide V_{gs} range. The noise level (in this case at $2f_{sig}$ or frequency of the second harmonic) is displayed in **Figure S1**a and S1b. Figure S1c shows, the rms noise integrated in the 4-40Hz bandwidth, which was used to calculate the DNR displayed in Figure 2d. Figure S1d shows the S/(D+N) ratio, a figure of merit that can be defined to show the impact of distortion on the signal quality for a wide $V_{gs} - A_{sig}$ range. The rms noise shown in Figure S1c was also used to calculate the S/(D+N) ratio.

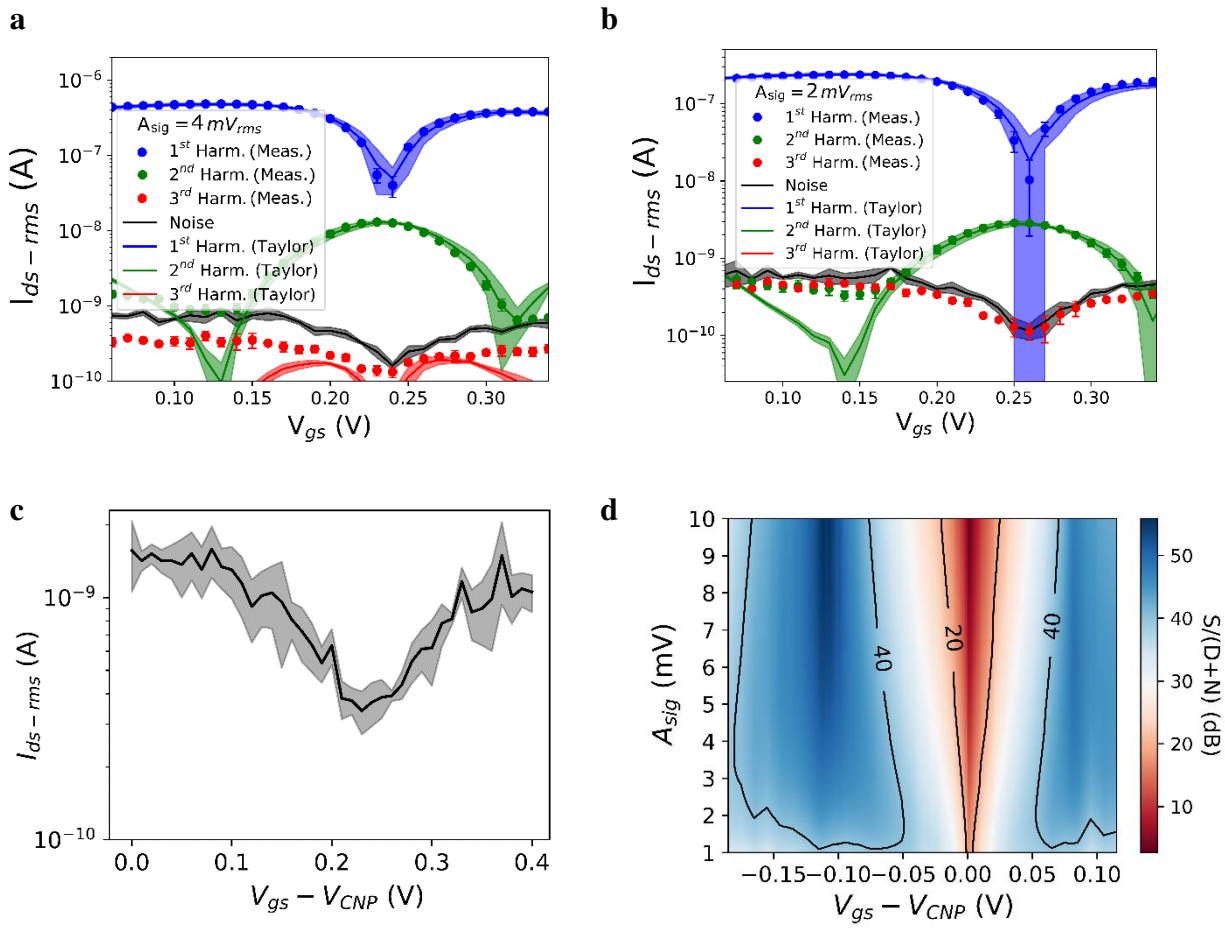

Figure S1: a) 1st, 2nd, and 3rd harmonics rms-amplitude extracted from the power spectrum of the measured I_{ds-sig} (dots-errorbar) and from the Taylor expansion of the $I_{ds} - V_{gs}$ curves (solid lines-filled area) for a signal amplitude A_{sig} of $4mV_{rms}$.. Error bars and filled area shows the standard deviation (n=4). The noise is evaluated from the power spectrum at 18Hz (i.e. slightly below $2f_{sig}$). b) The same as part a) for a signal amplitude A_{sig} of $2mV_{rms}$. c) The integrated noise in the 4-40 Hz is shown. These values were used to calculate the DNR in Figure 2d of the main text and Figure S1d. d) Signal to distortion plus noise in a wide $V_{gs} - A_{sig}$ range.

S2. Derivation of analytic transfer function

The derivation of the analytic transfer function describing the frequency response of the g-SGFETs is summarized in the main text. Here, the frequency dependence of the terms in Equation (1) of the main text are expressed explicitly.

The first factor in Equation (1) ($dI_{ds}/dV_{int}|_{V_{ds}}$), referred to as the intrinsic transconductance of the g-SGFET expresses how an electrical potential at the graphene-electrolyte interface couples with the channel conductivity, producing changes in the drain-to-source current. This

term is therefore proportional to the capacitance of the interface, which is usually considered independent of the frequency, as expressed in **Equation (S2)**.

$$G_m = \left.\frac{dI_{ds}}{dV_{int}}\right|_{V_{ds}} = V_{ds}\frac{W}{L}\mu\, C_{int} \tag{S2}$$

where W and L stand for the width and length of the channel respectively, and μ for the charge carriers electrical mobility. If the interface capacitance does not present an ideal capacitive behavior, but a constant phase element (CPE)-like response, a frequency dependent equivalent capacitance can be derived. Equating the imaginary part of the CPE impedance with the impedance of a pure capacitance the following equivalent capacitance (C_{CPE}) has been presented previously:[1]

$$C_{CPE} = \frac{Q_0}{\omega^{1-\alpha}}(\sin(\alpha\pi/2) - i\cos(\alpha\pi/2)) \tag{S3}$$

Where Q_0 is the inverse of the impedance at 1 rad/s and $(-\frac{\alpha\pi}{2})$ is the constant angle of its impedance in radians. Substituting **Equation (S3)** for C_{int} in Equation S2, the term regarded as "CPE dominated" in Equation (1) of the main text can be derived.

The second factor in Equation (1) of the main text (dV_{int}/dV_{gs}) represents the effect of the voltage divider composed by the impedance of the graphene-electrolyte interface and the resistance in series (R_s) which includes the contact resistance of the GFET (R_c) and the resistance of the electrolyte (R_{ele}). In addition, if there is a parasitic impedance in parallel with the graphene-electrolyte interface, it must be taken into account to calculate the attenuation of voltage drop at the interface (V_{int}) with respect to the signal applied (V_{gs}). This parasitic impedance could be dominated by either leakage through the metal contacts accidentally exposed to the electrolyte or through the capacitive coupling of the metal tracks with the electrolyte through the 2 μm thick passivation layer. A similar explanation to this cut-off frequency has been reported before.[2] This attenuation factor or voltage divider can be therefore expressed as:

$$\frac{dV_{int}}{dV_{gs}} = \frac{Z_{CPE_{g-e}}//Z_{CPE_{par}}}{Z_{CPE_{g-e}}//Z_{CPE_{par}} + 2R_s} \tag{S4}$$

where the factor of 2 multiplying R_s comes from the definition of CPE_{g-e} and CPE_{par} in the equivalent circuit shown in Figure 3 of the main text. Writing the frequency dependence in **Equation (S4)** explicitely:

$$\frac{dV_{int}}{dV_{gs}} = \frac{1}{1 + 2\,R_s\left[Q_{g-e}(2\pi f)^{\alpha_{g-e}} e^{i\frac{\pi}{2}\alpha_{g-e}} + Q_{par}(2\pi f)^{\alpha_{par}} e^{i\frac{\pi}{2}\alpha_{par}}\right]}$$

(S5)

Finally, an additional term contributes positively to the gain at high frequencies. The high interface capacitance causes a direct capacitive current between gate and source through the channel as well as through CPE_{par}. These capacitive currents are distributed to drain and source equally. This contribution can be expressed as:

$$G_{m_{eff}}(f_{sig}) = 1/(2Z_{CPE}) + 1/(2Z_{CPE_{par}})$$

(S6)

writing the frequency dependence of **Equation (S6)** explicitly, the last term in Equation (1) of the main text can be derived:

$$G_{m_{eff}}(f_{sig}) = Q_{g-e}(2\pi f)^{\alpha_{g-e}} e^{i\frac{\pi}{2}\alpha_{g-e}} + Q_{par}(2\pi f)^{\alpha_{par}} e^{i\frac{\pi}{2}\alpha_{par}}$$

(S7)

Merging Equation (1) in the main text, **Equation** (S3), (S5) and **(S7)**, the frequency dependence of the transfer function for g-SGFETs can be expressed as:

$$G_m(f) = \pm k\frac{Q_{g-e}}{(2\pi f)^{1-\alpha}} e^{i\frac{\pi}{2}(\alpha_{g-e}-1)} \frac{1}{1 + 2\,R_s\left[Q_{g-e}(2\pi f)^{\alpha_{g-e}} e^{i\frac{\pi}{2}\alpha_{g-e}} + Q_{par}(2\pi f)^{\alpha_{par}} e^{i\frac{\pi}{2}\alpha_{par}}\right]} + Q_{g-e}(2\pi f)^{\alpha_{g-e}} e^{i\frac{\pi}{2}\alpha_{g-e}} + Q_{par}(2\pi f)^{\alpha_{par}} e^{i\frac{\pi}{2}\alpha_{par}}$$

(S8)

where $\pm$ takes the positive value in the electron conduction regime and negative in the hole conduction regime (producing a 180° degrees phase shift). Q_{g-e} and Q_{par} stand for the inverse of the impedance at $1\,rad/s$ for the terms CPE_{g-e} and CPE_{par} respectively. **Equation (S8)** describes the effect of the CPE behavior on the frequency response, which causes a drop of

G_m with frequency to a fractional order (i.e. $G_m(f) \propto f^{1-\alpha_{g-e}}$). In this regime, the phase of the transfer function depends on α as $\pi/2\ (\alpha - 1)$. The second factor in the first term of Equation S8 describes the drop of V_{int} with frequency, which is responsible for a drop in the $G_m(f)$ magnitude together with a negative phase shift. Finally, the second term in Equation S8, corresponding to capacitive currents through CPE_{g-e} and CPE_{par}, which produce an increase in the $G_m(f)$ magnitude and a positive phase shift.

Fitting of the experimentally obtained Bode plot can be used to extract the relevant parameters modelling the frequency response of the g-SGFETs. The following table summarizes the parameters extracted from the fitting shown in Figure 3a of the main text:

	PBS 100mM	PBS 0.5mM
Q_{g-e}	$1.8\mu Fs^{\alpha-1}/cm^2$	$1.6\mu Fs^{\alpha-1}/cm^2$
$Area$	$10^{-8}m^2$	$10^{-8}m^2$
α_{g-e}	0.97	0.905
$k\ [V_{ds}\mu W/L]$	$5.10^{-3}m^2/s$	$4.10^{-3}m^2/s$
Q_{par}	$8nFs^{\alpha-1}$	$8nFs^{\alpha-1}$
α_{par}	0.65	0.6
R_s	$3k\Omega$	$240k\Omega$

Table S1: Parameters extracted from the Bode plot fitting in Figure 3a of the main text.

S3. Effect of leakage through metal contacts exposed to the electrolyte

The signal attenuation at high frequencies due to the voltage divider between CPE_{g-e} and R_s might be affected by the parasitic capacitance from a poor insulation of the metal contacts of the g-SGFETs. In order to determine whether this is the case or the impedance of the graphene-electrolyte interface dominates the attenuation in the transconductance, two sets of devices, with and without a part of the metal contacts exposed to the electrolyte have been characterized. The access length (L_{access}), which is defined as the distance between the end of the metal-graphene contacts and the uninsulated graphene channel can be defined as negative (i.e. -2 μm) in the first case and positive (1.5 μm) in the second. In **Figure S2**, the frequency response for

these two types of device is shown. First, it can be observed that at low frequencies (below $10kHz$) the CPE behavior dominates the frequency response with a $\alpha = 0.89$ (PBS concentration was equal to 0.5mM). In a second place, it can be observed that in the $3kHz - 40kHz$ band, the attenuation due to the previously described voltage divider dominates the frequency response. In this frequency range, the attenuation is more pronounced for the $L_{access} = -2\mu m$ due to increased parasitic currents.

It is interesting to note that despite the voluntary exposure of the metal contacts to the electrolyte, the frequency response is not dominated by the V_{int} drop term in the frequency bandwidth of interest for neural sensing (i.e. $< 10kHz$). The action potentials shown in Figure 4e in the main text were recorded with the devices corresponding to the Bode plot in Figure S2b (for $L_{access} = -2\mu m$).

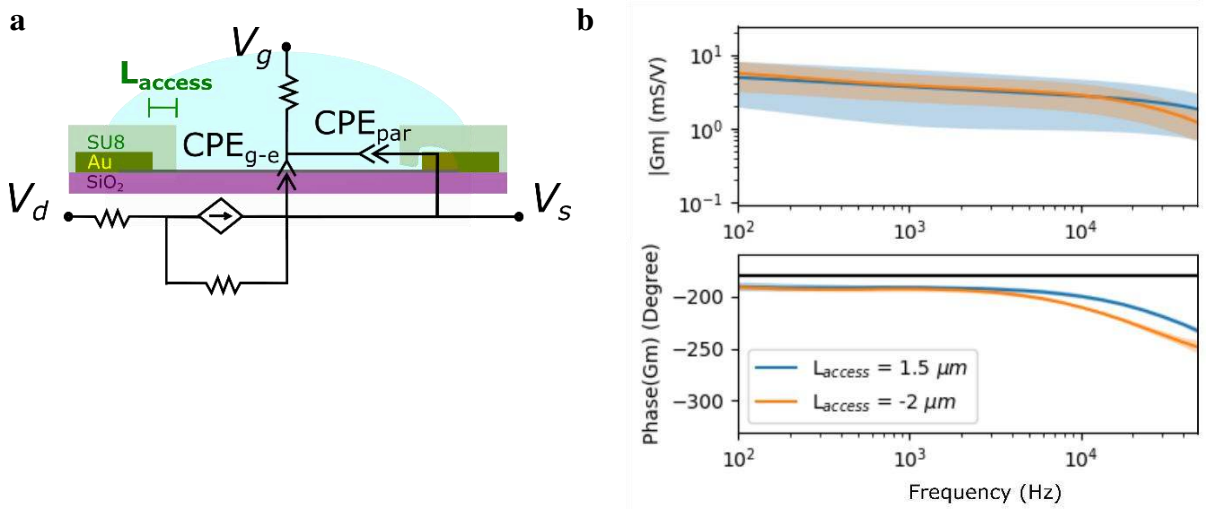

Figure S2: a) The equivalent circuit for the small signal model of the g-SGFET is schematized, indicating the meaning of L_{access}. b) The Bode representation for two different groups of g-SGFETs: with ($L_{access} = 1.5\mu m$) and without ($L_{access} = -2\mu m$) access region. The filled area indicates the standard deviation (n=4). The devices with $L_{access} = -2\mu m$ were used for HL-1 AP recording.

S4. Effect of impurities on the frequency response

It has been previously speculated that impurities on the graphene channel might play a crucial role in the CPE behavior of the graphene-electrolyte interface.[3] This dependence on the surface charge could also explain the dependence of the CPE behavior with the ionic concentration in the environment. **Figure S3**a shows the frequency response of a macroscopic g-SGFETs where the graphene was not processed after the transfer (i.e. the channel of the g-SGFET consists of the complete graphene layer transferred on the substrate and the passivation was done manually using epoxy). This device shows a flat frequency response, with a phase of $-180°$

(corresponding to the holes conduction regime). The increase of the G_m magnitude and phase for frequencies above $10Hz$ can be attributed to the capacitive currents described in the main text, which present a much larger contribution in this case due to the large area of the device (i.e. $5mm\ x\ 5mm$). The effect of contamination can also be observed from the effect of cleaning with ethanol the finalized devices fabricated using photolithographic means (see Figure S3b). The pronounced loss of G_m magnitude due to contamination is followed by an increased hysteresis in the $I_{ds} - V_{gs}$ curves and a doping of graphene which results in an increased minimum number of charge carriers and displacement of the CNP. The sign of the hysteresis (i.e. increase/decrease of the current for an increasing/degreasing voltage) confirms that it is caused by a slow charging of the interface capacitance.[4,5]

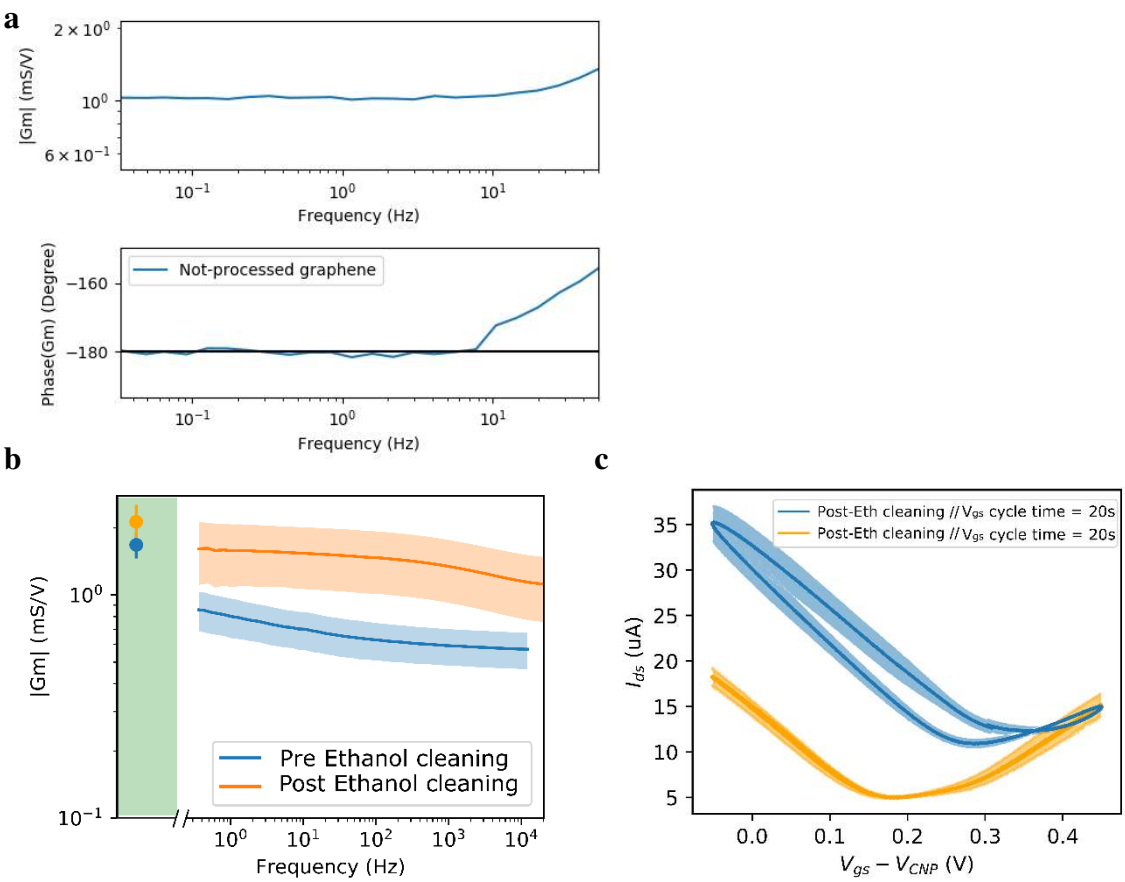

Figure S3: a) Bode representation of the macroscopic (unprocessesed) g-SGFET frequency response. b) Magnitude of the G_m over frequency for the processed g-SGFETs before and after cleaning with ethanol (n=4). c) Effect of cleaning with ethanol on the $I_{ds} - V_{gs}$ curves of the g-SGFETs. The filled area in all graphs indicates the standard deviation (n=4).

S5. Correction of harmonic distortion by interpolation into the $I_{ds} - V_{gs}$ curve

The schematic shown in **Figure S4**a illustrates the interpolation approach used to calibrate the signals. The distorted signal (dashed-red line) when interpolated into the $I_{ds} - V_{gs}$ curve is rescaled and the harmonic distortion simultaneously corrected. The resulting signal is shown by the solid-red line. The effect of calibration on the amplitude of the second harmonic is shown in Figure S4b for two different A_{sig} values. The three vertical lines in Figure S4b indicate the bias conditions for the spectra shown in Figure S4c. In Figure S4c it is possible to see that the increase of amplitude at $2f_{sig}$ around the CNP is due to calibrated noise level with small transconductance. The effectivity of the calibration method is also confirmed by showing the SDR (after calibration) on top of the A_{sig}-V_{gs} parameter map from Figure 2c in the main text. It is shown that the SDR is approximately flat over a wide V_{gs} range and its dependence with A_{sig} is effectively canceled.

The measured CSD events have been calibrated following the interpolation method. Afterwards, the calibrated signal corresponding to a quasi-distortion free signal has been artificially distorted for different V_{gs} values to show the effect of bias on the signal distortion (see Figure S4e). It is possible to observe a transition from a signal amplitude underestimation (for V_{gs} far away from the CNP) to a signal amplitude overestimation (close to the CNP). Figure S4f shows the difference in the CSD amplitude obtained by calibrating with a constant G_m and with the interpolation method. The error made in the signal amplitude determination by using a constant G_m becomes zero around $V_{gs} - V_{CNP} \approx -110mV$ where the impact of distortion is minimal as shown in Figure S4b and S4d.

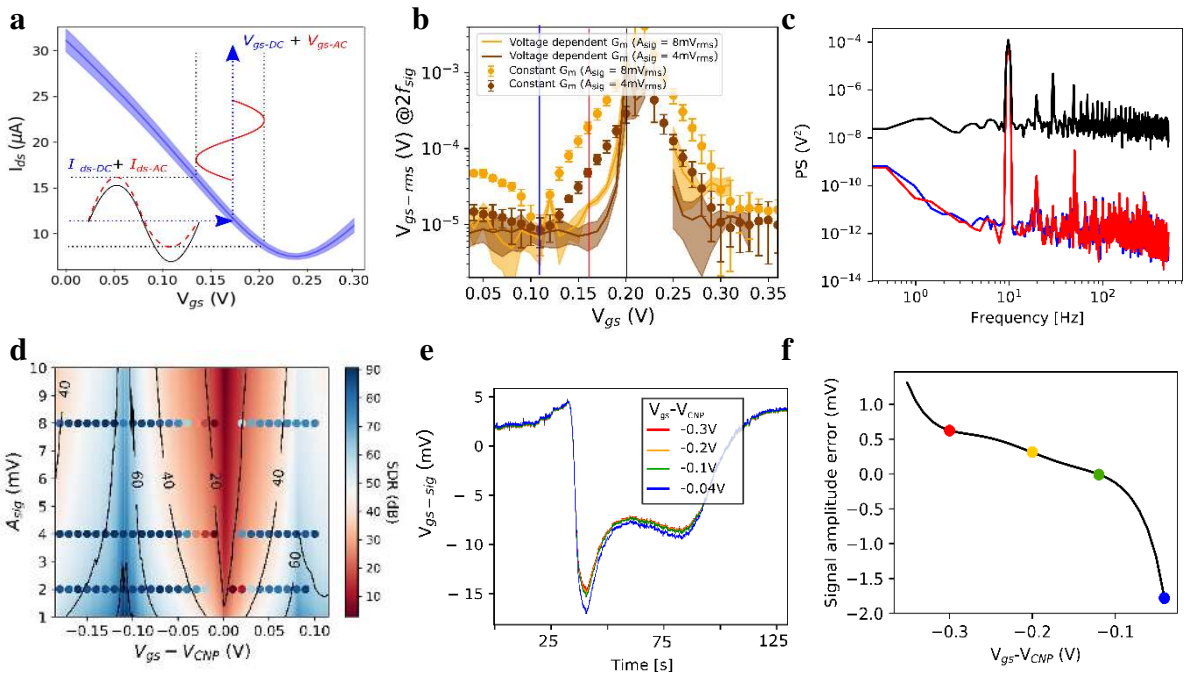

Figure S4: a) Scheme of the calibration approach. Input signal in current is interpolated into the $I_{ds} - V_{gs}$ curve leading to a calibrated signal in voltage with the harmonic distortions corrected. b) The amplitude of the second harmonic in the equivalent voltage at the gate is shown for $A_c = 8mV$ and $4mV$ and calibrated using a constant G_m (dots) and using the interpolation into the $I_{ds} - V_{gs}$ curves (solid lines). The errorbars and filled area show the standard deviation for n=4. c) Spectra at different representative V_{gs} values (marked by vertical lines in part b). The high SDR ratio close to the CNP appears due to an increase in the equivalent noise at the gate rather than an increase of higher orders. d) The SDR shown in Figure 2d is now plotted with the SDR after calibration with the non-linear $I_{ds} - V_{gs}$ curves. e) Effect of harmonic distortion on the recording of CSDs for different bias conditions. f) The error in the amplitude of the CSD due to harmonic distortion is shown for different V_{gs} values. The colored dots indicate the bias conditions corresponding to the CSD curves in part e).

S6. Limits in the static model of harmonic distortion

The slow charging of the graphene-electrolyte interface capacitance leads to a hysteretic response of the $I_{ds} - V_{gs}$ curve as shown in Figure S3c. The impact of the hysteresis on the harmonic signal distortion, which is related to a non-ideal frequency response, can be better evaluated by measuring harmonic distortion at different frequencies. To evaluate the impact of the non-ideal frequency response on the harmonic distortion, the comparison between measured harmonic distortion and calculated values from the Taylor expansion of the $I_{ds} - V_{gs}$ curve has been performed for a $1kHz$ pure tone. **Figure S5**a shows the result of this comparison; it is possible to observe a discrepancy between the DC and AC-derived values. This deviation for the 1st harmonic (corresponding to the applied signal) is proportional to the drop observed in the magnitude of the frequency dependent transfer function (ΔG_m shown in Figure S5a and

S5b). Interestingly, the 2nd harmonic and the 3rd harmonic drop by the same factor (ΔG_m) squared and cubed respectively. This attenuation corresponds to divide the signal at the interface (V_{int}) by a factor ΔG_m. The close match between the actual distortion and the values extracted from the DC characteristics after correcting the signal amplitude indicates that the hysteretic response does not change significantly the harmonic distortion (Figure S5c), but only the effective signal at the gate V_{int}.

This deviation from the stationary response, however, has a small impact for the calibration of electrophysiological signals. Signals with a large amplitude of few mV are typically in the slow frequency range and therefore close to the stationary response. A deviation from the transconductance of the measured $I_{ds} - V_{gs}$ curve and the actual transconductance at the frequency of the signals will cause a second order error in the signal amplitude determination.

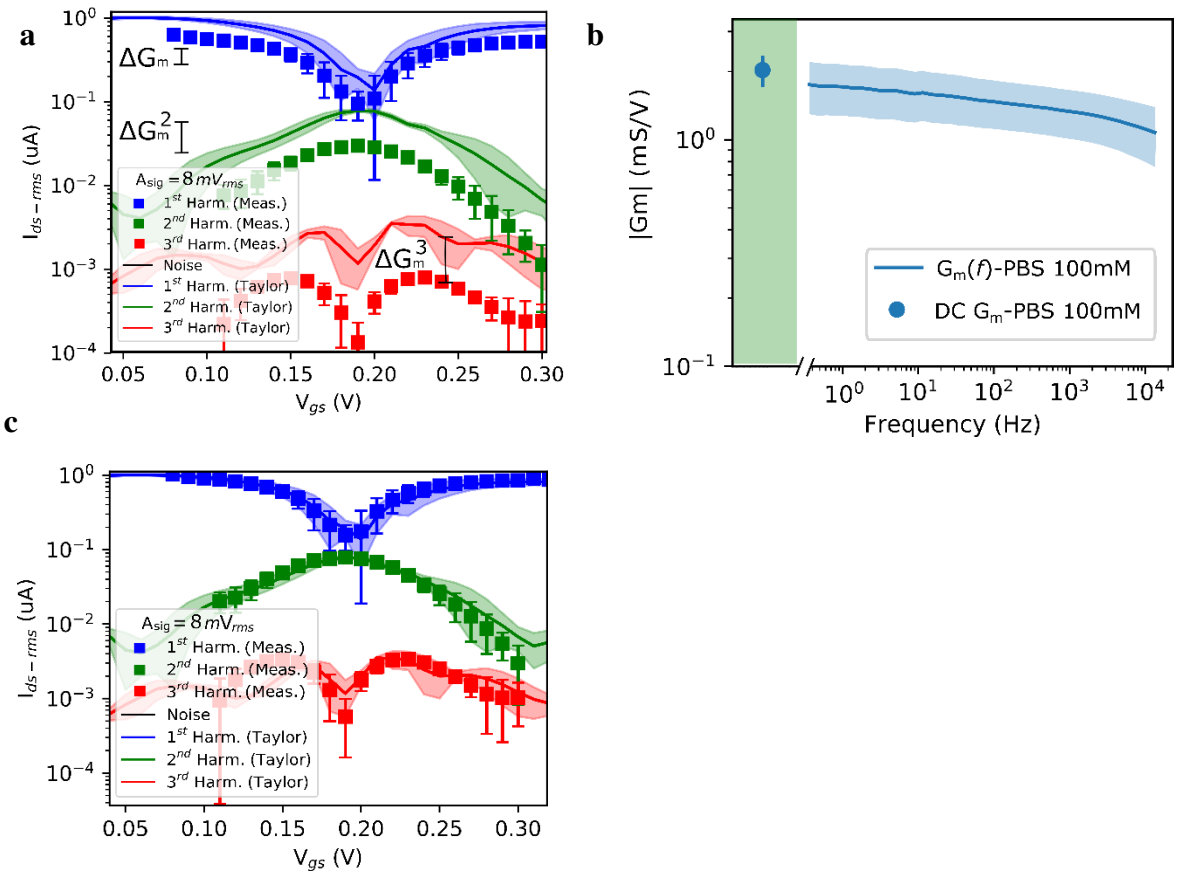

Figure S5: a) Comparison of signal amplitude, 2nd and 3rd order harmonics amplitude extracted from the Taylor expansion of the static $I_{ds} - V_{gs}$ curve and measured by applying a 1kHz pure tone signal at the gate. b) Magnitude of the G_m over frequency and DC G_m of the g-SGFETs used for the characterization of harmonic distortion shown in graph (a) and (c). c) Comparison of AC-derived harmonic distortion and the values extracted from the Taylor expansion of the $I_{ds} - V_{gs}$ curve corrected with the the frequency drop of C_{CPE} at $1kHz$. The errorbars and filled area in all graphs show the standard deviation for n=4.

S7. Numerical implementation of the analytic transfer function

To implement the transfer function of fractional order it has to be approximated as a higher (and integer) order system which mantains a constant phase over a certain bandwidth.[6] Figure S6 shows the approximation of the transfer function using Oustaloup's method which synthetizes the TF by the recursive distribution of $(2N+1)$ zeros and poles.[7] This method gives an accurate description of the non-integer order TF within a defined bandwidth $[\omega_b, \omega_h]$ (see **Figure S6**). In addition, it has the advantage over other modelling tools that its digital implementation for real-time applications is given in a straight forward manner from its finite number of zeros and poles.

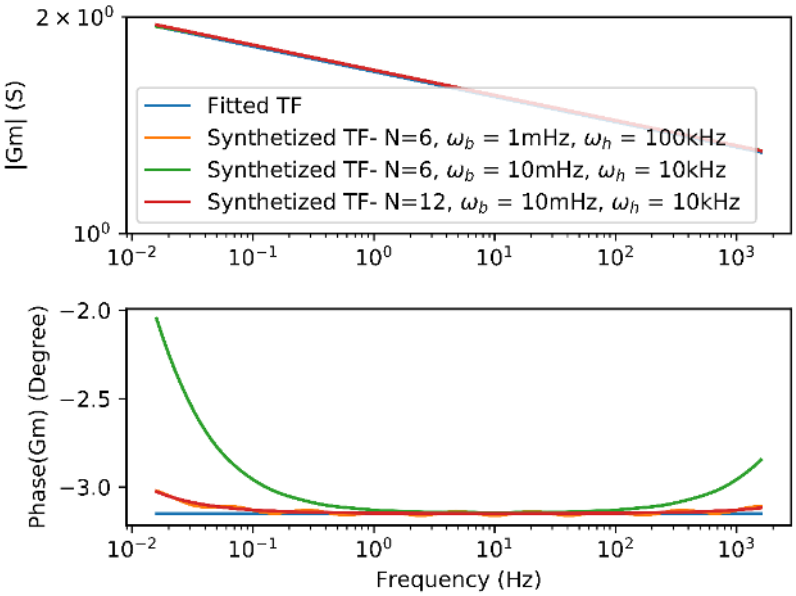

Figure S6: Analytical transfer function (blue) and approximated TF using Oustaloup's method for different bandwidths and number of poles and zeros.

References

[1] C. H. Hsu, F. Mansfeld, *CORROSION* **2001**, *57*, 747.

[2] C. Mackin, L. H. Hess, A. Hsu, Y. Song, J. Kong, J. A. Garrido, T. Palacios, *IEEE Trans. Electron Devices* **2014**, *61*, 3971.

[3] J. Sun, Y. Liu, *Nanomaterials* **2019**, *9*, 923.

[4] H. Wang, Y. Wu, C. Cong, J. Shang, T. Yu, *ACS Nano* **2010**, *4*, 7221.

[5] M. Winters, E. Ö. Sveinbjörnsson, N. Rorsman, *J. Appl. Phys.* **2015**, *117*, 074501.

[6] S. Das, I. Pan, *Fractional Order Signal Processing*, Springer Berlin Heidelberg, Berlin, Heidelberg, **2012**.

[7] A. Oustaloup, F. Levron, B. Mathieu, F. M. Nanot, *IEEE Trans. Circuits Syst. I Fundam. Theory Appl.* **2000**, *47*, 25.